2018 SCEC Report

Award Number 18038

Collection of very high-resolution topography along the southern San Andreas Fault to resolve slip distribution in recent surface ruptures: Towards automated recognition and analysis of fault zone geomorphic features

Principle Investigators:

Thomas Rockwell

Allen Gontz

San Diego State University

TOTAL AMOUNT OF AWARD: $15,000

PROPOSAL CATEGORY: **Data Gathering and Products**

DICIPLINARY ACTIVITY: **Earthquake Geology**

SCIENCE OBJECTIVES: **1a, 5d, 5c**

Introduction

This past year, we collected very high-resolution aerial imagery along selected portions of the southern San Andreas fault (sSAF) (Figure 1), with the purpose of mapping offset rills, stream channels, alluvial bars and other features that can be used as piercing points. Our goal has been to develop quantitative information about displacement in past sSAF earthquakes. We targeted six sub-areas from the Indio Hills to the Mecca Hills in our initial surveys, testing the best flight altitude to achieve the desired resolution, with a seventh site at Salt Creek. We found that collecting data at about 25 m above ground level (AGL) produced imagery with sub-cm resolution (~7-8 mm) from which we can map out even very small deflections and offsets along the fault. The imagery is spectacular; and small offsets ranging from tens of cm's to tens of m's are clear and convincing (Blanton et al., 2018a; Blanton et al., 2018b).

Figure 1. *Map showing the sections of the southern San Andreas fault that we surveyed this past year, along with the many paleoseismic sites with which we will integrate offset observations.*

During our initial field campaigns last winter, we identified clear evidence of a very recent creep event and mapped 2.7 km of surface cracking with up to 1.4 cm of lateral displacement southeast of Box Canyon Road, just to the south of Mecca Hills (Figures 1 and 2). We also identified minor cracking at several other locations, including next to Roger Bilham's creep meter at Salt Creek. This led to an investigation into this creep episode using InSAR (Fialko's group), creep-meter data (R. Bilham), and surface crack mapping (Rockwell/Gontz's group), which resulted in the submission of a paper to JGR this past fall (Tymofyeyeva et al., 2018 in review, about to be resubmitted). We continued to work in the Mecca Hills area through the spring and into the first half of the summer and saw no new evidence of surface creep. However, renewed flights in the northwestern Mecca Hills in late September and early October identified fresh cracking. These observations have demonstrated that a creep event started in the south immediately after the 2017 M8 Chiapas earthquake and has been working its way to the northwest, reaching the NW end of the Mecca Hills by September/October 2018, although the

October 12, 2018 storm erased the new cracking in the NW Mecca Hills, as well as probably farther SE. One important aspect that is relevant to our UAV surveys is that the rupture associated with the creep event allowed us to define the principal slip surface for much of the fault in the areas that we worked, which in turn allowed us to confidently identify small, sub-meter offsets that have resulted entirely from creep, as discussed further below.

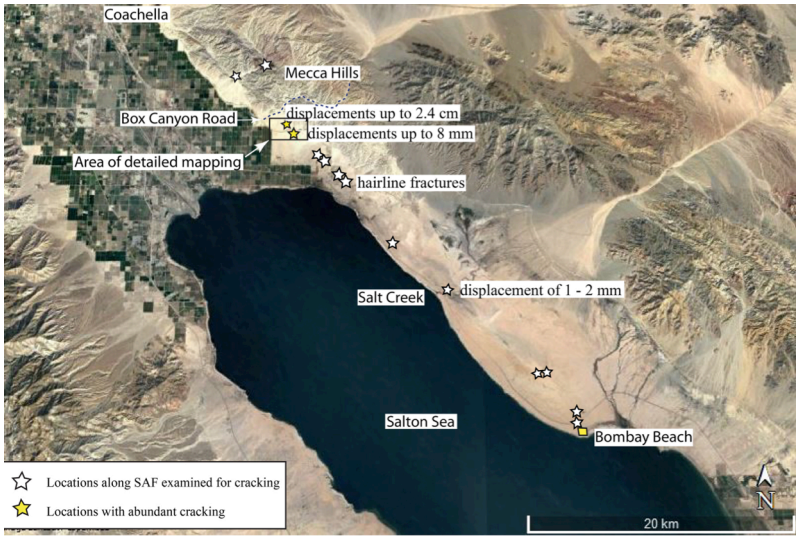

Figure 2. *Map of 2018 surface creep measurements along the southern SAF (Tymofyeyeva et al., 2018 in review).*

In the following sections, we present a portion of the collected imagery and the interpretations derived from the new imagery for the Mecca Hills flight sections. This work, which comprises the MS thesis product of Chelsea Blanton, will soon be submitted for publication.

Study Sites

After collection and preliminary analysis of the initial flight survey areas, we focused field work on those flights in the Mecca Hills because they were rich with offset rills and channels, which we call sites 1 and 2. Site 1 is near Mecca, California in Box Canyon approximately 1 km southeast of Box Canyon Road and about 0.5 km northwest of the Coachella Canal: this is termed the "South Mecca Hills Survey Area" in Figure 1. This site is the same area where Dingler et al. (2016) collected a comprehensive 3D dataset using terrestrial laser scanning technology, and where Shifflett et al. (2002) measured gulley offsets and identified an offset Native American "fire ring". Site 2 is near Thermal, California and is less than 0.5 km southeast of Thermal Canyon within the property of an open pit mine operated by West Coast Sand and Gravel, Inc., shown as "Mecca Hills with 4 sub-areas of Survey" on Figure 1. Both areas have many good offset features and were chosen for our main focus because the Box Canyon site is southeast of where the SAF splays into multiple strands, whereas the Thermal site is northwest of where most or all slip has re-coalesced back onto the main strand of the SAF. The Indio Hills and Salt Creek survey areas will be further evaluated with additional flights in future work.

Methods

Data Collection - Initial fieldwork consisted of locating sites via Google Earth imagery that had good potential for rill formation that could capture small offset features and assessing those sites in the field. Nine fault sections were evaluated during a walk through and those having areas with steep slopes, well-preserved geomorphic offsets, and accessibility with an off-road vehicle were selected for surveying. Real time kinematic (RTK) GPS surveys and UAV surveys were conducted at each site, in addition to collection of field measurements of offset rills and channels with a standard metric tape measure.

At Box Canyon ground control points (GCPs) were placed at the four corners of our area of interest prior to the UAV surveys. This RTK GPS system was on loan from Geodetics Inc., San

Diego with several operators and they were responsible for collection of GCPs for our four Box Canyon flights. Two additional GCPs were manually added later during processing using GPS coordinates extracted from Google Earth for two archeological stone rings apparent in the area. For our Mecca Hills sites, GCPs were scattered along the fault on either side of the fault trace. GPS data were collected with an EMLID Reach RS RTK GPS for each GCP used in the Mecca Hills flights. The rover and base stations were setup in RTK mode with a correction link over Lo-Ra (Long Range) radio. The kinematic positioning mode, which assumes the receiver is moving, and the fix-and-hold ambiguity resolution (AR) mode were utilized with the GLONASS AR mode enabled. The average single position base setup method was implemented to obtain base station coordinates with approximately 2.5 m accuracy. This approach is sufficient for this study as absolute accuracy is not required, only relative accuracy. The fix status was exercised during survey point collection, which provides cm-level precision between the relative position of the rover to the base station. For all base setup methods, the relative position of the rover will be cm-precise while using the fix status to collect GCPs; however, the actual accuracy will be set by the accuracy of the base station position. Therefore, methods with longer observation times, 15 minutes to four hours compared to five minutes, were deemed unnecessary.

Approximately 500,000 m^2 of aerial imagery, consisting of over 4,300 images, was collected via UAV surveys along the SAF. A portion of this imagery is an ~1.7 km continuous segment of the fault with an average swath width of 95 m. Two UAVs were utilized in flight missions to collect this aerial imagery. A DJI Matrice 600 Pro (M600 Pro) was used at the Box Canyon site. The camera onboard the M600 Pro was a Sony Alpha 6000 (model ILCE-6000) with a focal length of 16 mm and 6000 x 4000 image pixel resolution. The M600 Pro equipment was on loan from Geodetics Inc., San Diego with a pilot who was responsible for all flight operations involving the M600. These flights were conducted using automated flight mapping application Maps Made Easy on an iPad and images were stored directly on the UAV's camera. A DJI Phantom 4 Pro was applied at all other sites in the Mecca Hills. The Phantom's onboard camera, DJI FC6310, has a focal length of 8.8 mm and 4864 x 3648 pixel resolution. While the DJI GO 4 application allows for systems checks and updates, it does not have an option for automated flight, so the automated flight mapping application "Drone Deploy" was used on a Samsung Galaxy S6 smart phone. All flights were set to a speed of 3 m/s with the obstacle avoidance enabled in addition to 75% frontlap and 65% sidelap for image capture, with images stored on the UAV's micro SD card. All automated UAV surveys, 9 in total (Table 1), were flown over the area of interest during peak sun hours (11am to 1pm) to diminish shadow effect. The altitude AGL is determined from the takeoff point, meaning the UAV does not automatically adjust to the local topography, so the UAV may be much closer to ground level for portions of the flight depending on the elevation of the terrain. Therefore, it was necessary to increase the altitude of several flights, so that the UAV would not encounter obstacles at any point throughout the flight. Flight details are shown in Table 1.

Flight Path	AGL (m)	Date of Flight(s)	UAV System	Coverage Area (m^2)
Box Canyon 1-4	30	2/23/2018	M600 Pro	92,100
Open Pit Mine 1	30	5/23/2018	DJI P4P	34,500
Open Pit Mine 2	25	5/23/2018	DJI P4P	43,500
Open Pit Mine 4	30	10/6/2018	DJI P4P	39,000
Open Pit Mine 5	30	10/6/2018	DJI P4P	50,200
Open Pit Mine 6	25	10/7/2018	DJI P4P	30,700

Table 1 *Details of the 9 Mecca Hills flights, with flight altitude above ground level (AGL) in meters, date the flight was conducted, UAV system used to conduct the flight, and flight area of coverage in square meters.*

Displaced small-scale geomorphic features are abundant along the ~1.7 km continuous fault segment at the open pit mine and along ~250 m of the ~700 m segment in Box Canyon. After UAV and RTK GPS surveys at each site, offset features were recorded along the fault with a tape measure, using the

distance between displaced channel thalwegs or channel margins as piercing points where we projected these features into the fault. Uncertainty was determined for each offset depending on the width of the measured feature and how well the feature was preserved in the field. An offset quality of poor, fair, good, or excellent was also assigned to each feature (Table 2). This was determined based on quality, preservation, and erosion level of the feature. Cracking due to lateral creep along the section of the sSAF at Box Canyon (Tymofyeyeva et al., 2018 in review) and at the open pit mine provided confirmation for the precise location of the main trace of the fault, which assisted in differentiating deflected and offset features. Additional GPS data were collected to record cracking using the US Topo Maps application with an accuracy of ± 2-4 m.

Image processing - After image collection, all imagery was processed the same. Dark or oblique images were removed from the photoset manually and the remaining images imported into SfM software Agisoft PhotoScan Professional, where the *Agisoft support Orthomosaic and DEM Generation with Agisoft PhotoScan Pro 1.3 (with GCPs) tutorial* (Support Beginner Level) was used to guide the generation of a georeferenced dense point cloud, digital surface model (DSM) and orthomosaic for each area. DSMs and orthomosaics were exported as a geoTIFF and TIFF, respectively, for post-processing in the WGS 84/UTM zone 11N coordinate system. One site was selected (Open Pit Mine 2) for processing at every quality level for the dense point cloud (low, medium, high, and ultra-high). It was determined that processing on high was adequate to observe decimeter-scale offsets and this setting decreased processing time and computational power dramatically. Each flight's parameters were set to high for photo alignment accuracy and high for dense point cloud quality (Figure 4).

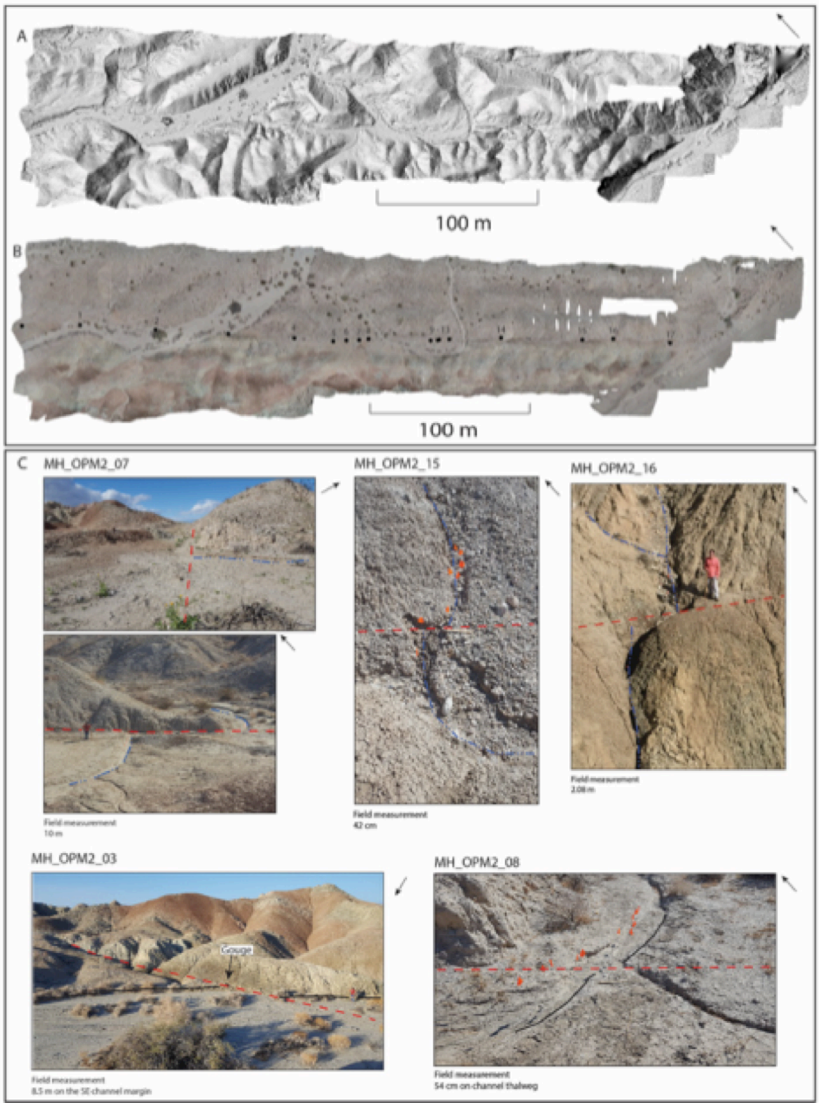

Figure 4 *Open Pit Mine 2, with hillshade (A) and orthomosaic (B) products for the flight, respectively. Black dots on the orthomosaic represent offset locations and values are the site numbers. C) Sample field measurements from OPM2. Black lines are channel margins, dashed blue lines channel thalwegs, and dashed red lines the surface trace of the SAF.*

The resulting

ground resolution of the imagery collected in the Mecca Hills and Box Canyon ranges from 0.489 cm/px to 0.859 cm/px. However, it is important to note that some images are captured closer to the ground than others due to the terrain. Therefore, the ground sampling distance (GSD) calculated from the image pixel width and height, focal length, sensor width, and altitude AGL, and distance from the camera to the object on the ground yields a slightly lower resolution for each flight. These two values are likely the maximum and minimum ground sampling distances for each site with the geoTIFF ground resolution as the maximum and the calculated GSD as the minimum. The changing terrain also explains why there are holes in some off-fault areas of the DSMs and orthomosaics. High resolution, low elevation flights provide higher visibility of small-scale offsets, but with closer proximity to the ground surface, the overlap between images becomes insufficient at elevation peaks. Agisoft will disable, and thus exclude from photogrammetric processing, images with inadequate tie points.

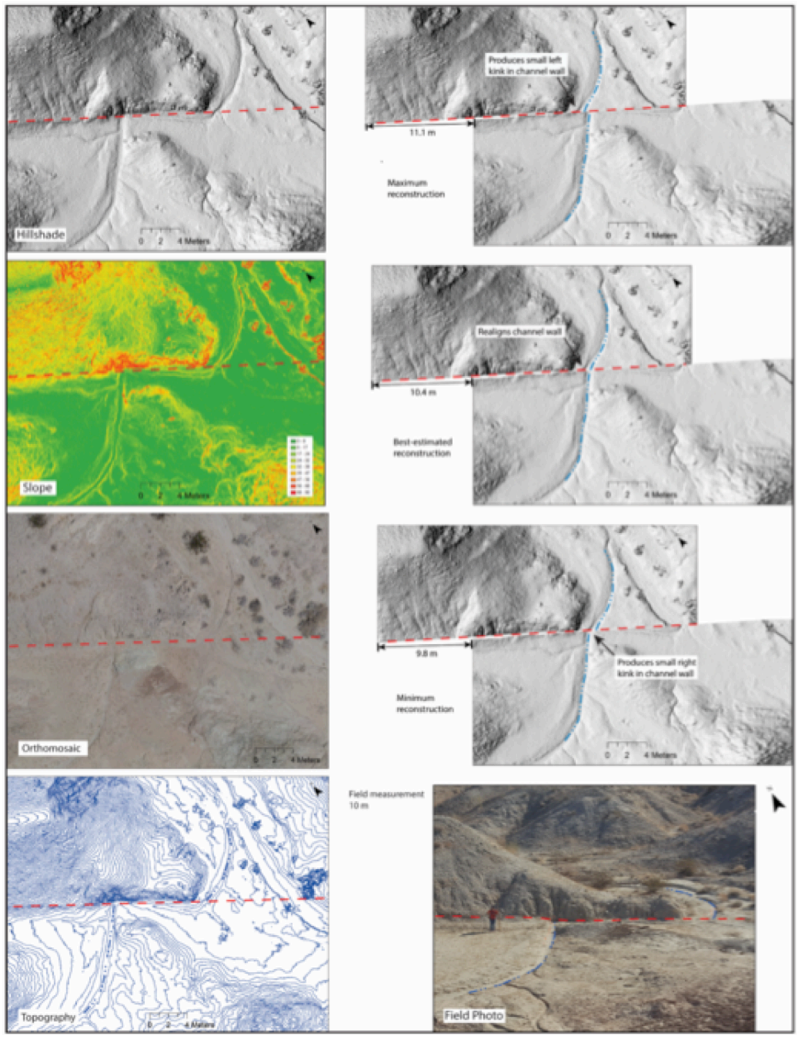

Figure 5 *The series of images on the left, from top to bottom, are the hillshade surface map, slope surface map, orthomosaic, and topographic map of the offset feature MH_OPM2_07. The degree of slope is shown by a color map that represents flat surfaces as green, shallow slopes as yellow, moderate slopes as light to dark orange and steep slopes as red. Annotated blue lines represent the channel thalweg, black lines show channel margins, and red lines depict the surface trace of the SAF. The series of images on the right show, from top to bottom, maximum, best-estimated, and minimum offset reconstructions produced with the hillshade map and a field photo of the offset.*

Additionally, depending on the quality selected for dense point cloud generation, image down-sampling may occur. The ultra-high-quality setting processes original photos (the DSM would have the same resolution as the ground resolution), while each lower quality setting implies preliminary image size downscaling by a factor of 4 (Agisoft PhotoScan User Manual Professional Edition, Version 1.4). This process decreases the resolution of the DSM. Therefore, the selected dense point cloud processing quality (high) lowers the DSM resolution for our processed flights. Nevertheless, the resulting orthomosaic resolution remains equal to the high ground resolution .

Interpretation and Analysis - The DSMs were imported into ArcGIS and used to create hillshade and slope surface raster coverages using the hillshade and slope tools in ArcGIS, which enhanced our visualization capabilities of the ground surface. Various parameters were tested for

the hillshade and a 315 degree azimuth (northwest orientation of the sun) and 55 degree altitude produced a hillshade product that best enhanced landscape features of interest. Topographic maps were also generated at 1 m, 10 cm, and 5 cm contour intervals to highlight small-scale offset features.

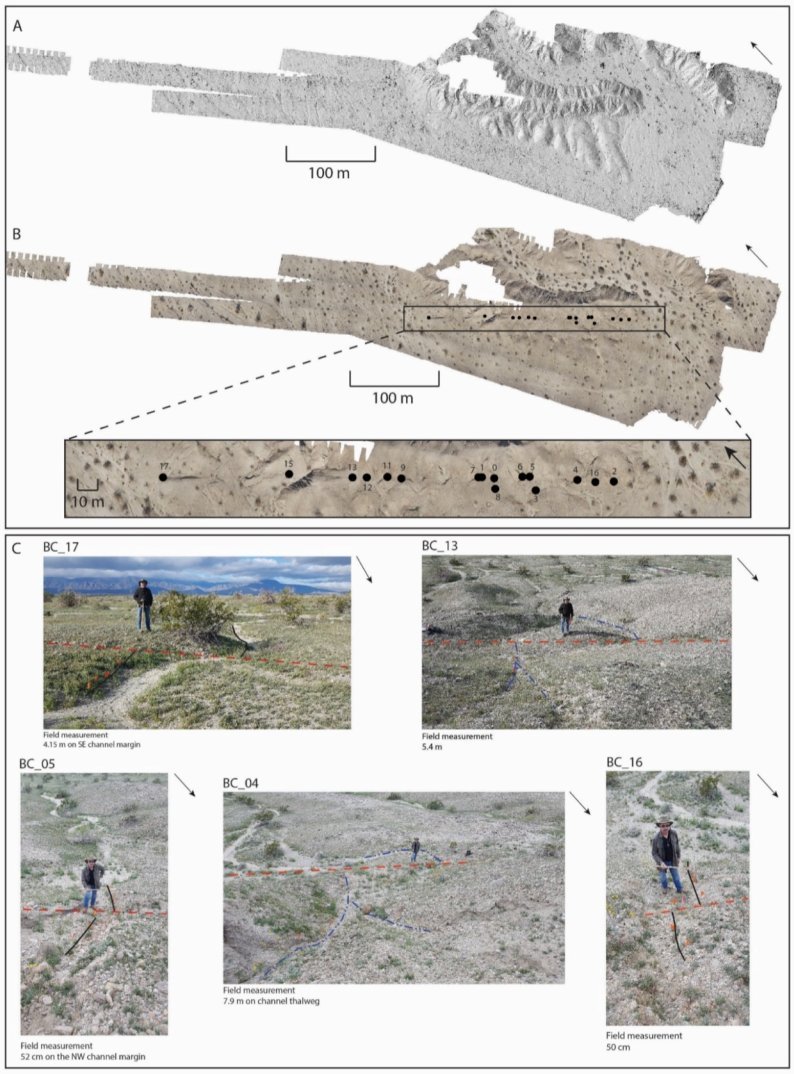

Figure 6. *Box Canyon flights. Hillshade (A) and orthomosaic (B) products for the flighst, respectively. Black dots on the orthomosaic represent offset locations and values are the site numbers. C) Sample field measurements from BC. Black lines are channel margins, dashed blue lines channel thalwegs, and dashed red lines the surface trace of the SAF.*

The fault trace was then annotated on the hillshade in ArcGIS and the many offset features located. To verify field measurements greater than 1 m, hillshade and slope surface rasters were transferred to Adobe Photoshop as JPEGs and offset features were reconstructed to their inferred original configuration. This was done by slicing in Photoshop along the fault trace, putting the divided products in separate layers, and moving these layers along the fault until the offset feature was realigned (see reconstructions in Figures 5 and 7). The maximum and minimum reconstructions served a secondary purpose of providing an approximate uncertainty value to the offset measurement.

A comparison of field measurements to measurements extracted from Agisoft (orthomosaic) and ArcGIS products (hillshade, slope, and topography maps) was conducted to understand the accuracy, precision, and uncertainty as it relates to each method. Two hillshade maps were generated, one at an azimuth of 315 degrees and altitude of 55 degrees (best) and another with an azimuth of 135 degrees and altitude of 55 degrees (user error), to evaluate how light direction influences geomorphic offset measurements. Moving forward, these surface maps will be referred to as hillshade 315 and hillshade 135. A Gaussian distribution analysis was completed in Microsoft Excel for each type of measurement, separately for the Mecca Hills and Box Canyon locales.

Results, Mecca Hills Survey Areas

Observed offsets range from 15 cm to 85 m for a total of 75 measurements, with 24 at Box Canyon and 51 at the Mecca Hills sites . Hillshade 315 maps, orthomosaics, and offset locations are shown for

Open Pit Mine 2 and Box Canyon with several example offsets (Figures 4 and 6). An offset example for each of these sites is provided to illustrate each type of measurement, including hillshade 315, slope, orthomosaic, topography, reconstruction, and field measurements (Figures 5 and 7).

Discussion

Data Analysis - On average, best-estimated reconstruction measurements are greater than those measured in the field. Hillshade 135 measurements are about equal to or slightly greater than those measured in the field. Orthomosaic, hillshade 315, slope, and topography measurements yield inconsistent results showing greater variation when compared to the Hillshade 135 and field measurements. These measurements tend to be greater than the field measurements for the Mecca Hills sites and less than the field measurements for Box Canyon. The coefficient of determination (R^2) values resulting from correlation plots comparing field measurements to measurements extracted from surface maps range from 0.9593 to 0.9937 , so the various measurement methods are generally in agreement within fifteen percent uncertainty. As the topographic maps are based directly on the elevation of the DSMs, we interpret that the measurements extrapolated from them are the most accurate to use in conjunction with field measurements and are susceptible to the least amount of bias, as the thalwegs of offset

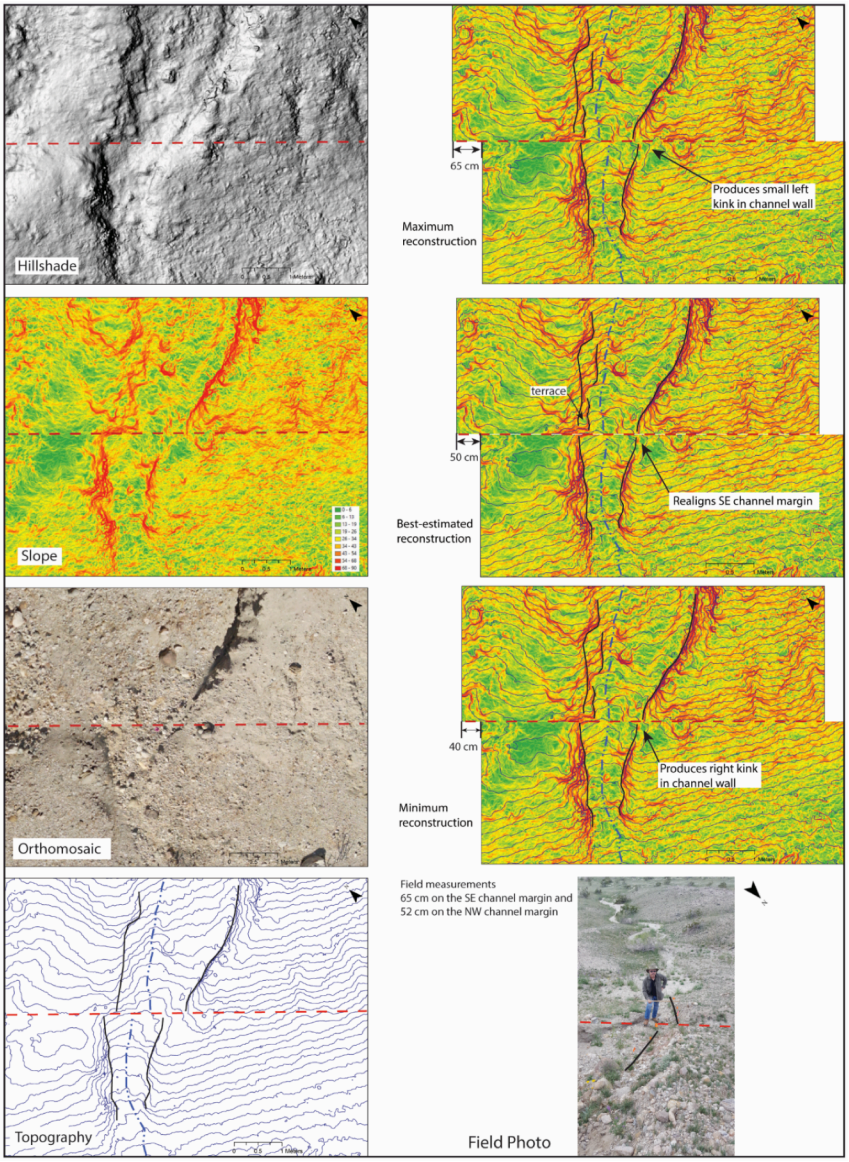

Figure 7. *The series of images on the left, from top to bottom, are the hillshade surface map, slope surface map, orthomosaic, and topograpic map of the offset feature BC_05. The degree of slope is shown by a color map that represents flat surfaces as green, shallow slopes as yellow, moderate slopes as light to dark orange and steep slopes as red. Annotated blue lines represent the channel thalweg, black lines show channel margins, and red lines depict the surface trace of the SAF. The series of images on the right show, from top to bottom, maximum, best- estimated, and minimum offset reconstructions produced with the slope map and a field photo of the offset.*

geomorphic features are clearly represented by the topography.

As is seen in the stacked Gaussian distribution analyses for Mecca Hills (Figure 8) and Box Canyon , cluster values are generally in agreement for each measurement method for meter-scale offsets and decimeter-scale offsets at Mecca Hills. The offset data for Box Canyon results in misalignment of cluster values for the decimeter-scale offsets at this site between different measurement methods, but meter-scale offsets still agree well. Furthermore, a reconstruction was not completed for every offset feature at MH and BC, so the best-estimated reconstruction summation at each site has significant separation from the general summation trend because this method has approximately 50% of the measurement density in comparison to all other methods. Gaussian distribution analysis reveals offset clusters at about 20 and 50 cm in the field and topography measurements at both Mecca Hills and Box Canyon. As the offsets increase in size, and therefore uncertainty, the data becomes more broadly distributed. An additional peak at about 130 cm in the Mecca Hills topography data is the result of one measurement and is therefore not interpreted because it does not show up anywhere else.

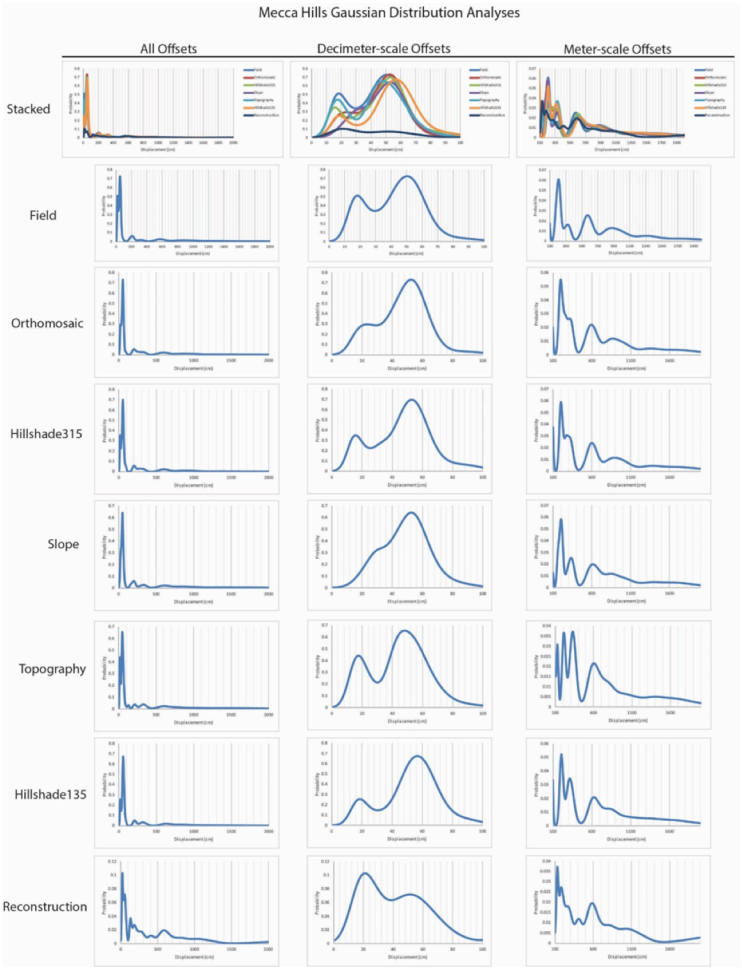

Figure 8. *Gaussian distribution of the 51 offset features in the Mecca Hills study area divided by measurement type with the columns showing all offsets, decimeter-scale offsets, and meter-scale offsets. Stacked profiles show all measurement method slip signals.*

Paleoseismic Interpretation

To assess slip per event, measurements were divided into groups based on similar offset values, with Box Canyon and Mecca Hills slip per event calculated separately between field and topographic measurement data. We calculated the mean of each group, and each group was assigned an earthquake age in order to correct for creep of ~3 mm/yr (as previously determined by our small-scale offset data). The difference between the mean displacement of each group yields the average slip per event in meters following the method established in Rockwell and Pinault (1986) and assuming each group represents a specific event. Event dates for the most recent surface-rupturing event (MRE) and penultimate event are from Rockwell et al. (2018), and successive median earthquake dates are from Philibosian et al. (2011). Two different groupings were applied to evaluate

the data: 5 events and 4 events. The 5-event model represents an earthquake for each resulting peak of the Gaussian distribution, while the 4-event model suggests some bimodal displacement behavior of the MRE (as described in Weldon et al., 1996). To compare the inferred average slip rate derived from our data to longer-term rates established for the southern SAF (Behr et al., 2010; van der Woerd et al., 2006), we used the largest grouped offset value and the oldest estimated earthquake event [slip rate = (greatest offset in m/oldest earthquake event in ka) * 1000]. This slip rate includes components of creep, triggered offset, and co-seismic offset, not accounting for lateral variations in displacement and excluding off-fault deformation. In the 5-event model, the slip per event values range from 0.4 to 5.8 m with an average slip per event of 2.1-2.2 m at Box Canyon. At Mecca Hills the slip per event is estimated at 0.7 to 4.4 m with an average slip per event of 2.0-2.1 m . The resulting slip rates are 15.1 – 15.8 mm/yr and 14.6 – 15.1 mm/yr for Box Canyon and Mecca Hills, respectively. The 4-event model yields slip per event values of 1.7 to 5.9 m with an average slip per event of 2.8-2.9 m at Box Canyon, and slip per event of 1.5 to 4.5 m with an average slip per event of 2.7-2.8 m at Mecca Hills (Table 2). Inferred slip rates are 18.5 – 19.3 mm/yr and 17.9 – 18.5 mm/yr at Box Canyon and Mecca Hills, respectively, which better agree with the long-term geologic rates.

Meter-scale offsets represent one or multiple earthquakes along the southern segment of the SAF. Uncertainty is largest for the greatest offset features and least for smaller scale features. Older offset features with greater displacements are less abundant than more recent offsets due to younger earthquakes. The combination of older and younger offsets within the same section of the fault implies that the past several earthquakes likely ruptured the surface at approximately the same length of the fault (Rockwell and Pinault, 1986). As the southeast section of the SAF at Box Canyon transitions from single-stranded to double-stranded locally, total slip was probably not measured, so the measurements along the main trace of the double-stranded section reflect only minimum slip. Each Gaussian peak likely represents the cumulative slip associated with the past five earthquakes. If bimodal behavior of the first two peaks is considered, the observed peaks may represent the cumulative slip of the four most recent clusters of earthquakes, each consisting of a single large earthquake, smaller size earthquakes, and accumulated creep and triggered slip (Zielke et al., 2010). Based on this bimodal behavior, we suggest that the 4-event model is the most likely scenario.

Event	Mecca Hills Slip	Box Canyon Slip	Years Since the Previous Event
1726 ± 7	1.5-1.8	1.9-2.0	149
1577 ± 67	2.9-3.0	1.7-1.9	157
~1420	1.9-2.8	1.9-2.6	120
~1300	3.5-4.5	4.9-5.9	160

Table 2. *Resulting slip per event data in meters for the last 4 earthquakes on the southern SAF according to the 4-event model. Average earthquake dates are used to determine the time since the previous event. Event dates from Philibosian et al. (2011) and Rockwell et al. (2018).*

Intrinsic variability and measurement uncertainty in this study undoubtedly have a significant effect on the cumulative distribution of lateral offsets and result in a muted signal in offsets with increased slip and uncertainty (Weldon, McCalpin, and Rockwell, 1996). Therefore, an older event may not be apparent in the data; for example, offset measurements of about 17 and 21 m at Mecca Hills show no signal in the Gaussian distribution analysis. Displacement estimates for this model indicate that the MRE produced an average of 1.5-2 m of dextral slip with maximum slip of 2 m at Box Canyon (Table 2). This displacement is significantly less than the purported 3.75 m of slip attributed to the MRE in Dingler et al. (2016), which occupies the same site at Box Canyon. Between our two sites, approximately 12 km apart, there is a greater amount of slip observed for the penultimate event at Mecca Hills and a larger amount of slip at Box Canyon for event 4 . If we consider the multi-stranded nature of the fault at Box Canyon, it is likely that slip is distributed between both strands of the fault.

Therefore, it may only appear that the Mecca Hills accommodated greater slip in the penultimate event.

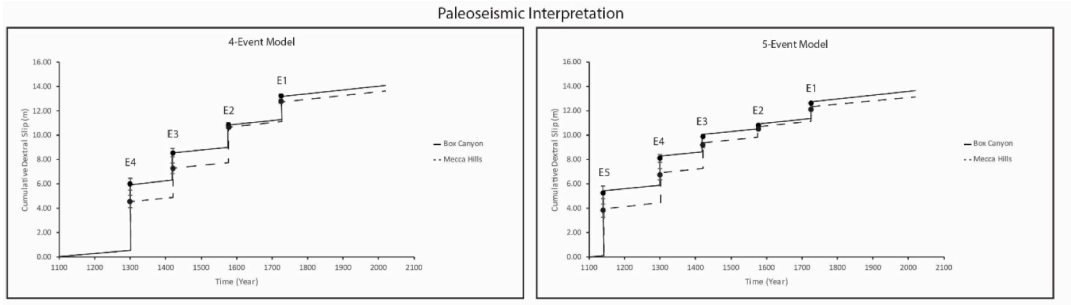

Figure 9. *Time series diagram showing the cumulative dextral slip over time at Box Canyon and Mecca Hills for the 4-Event and 5-Event models. E1 – E5 show estimated earthquake ages according to paleoseismic studies (Philibosian et al., 2011; Rockwell et al., 2018). Slip distances are from the slip per event data in this study based on our offset measurements. Creep is assumed at a rate of ~3 mm/yr.*

The 4-event model yields minimum to maximum slip rates of 17.9 – 18.5 mm/yr at Mecca Hills and 18.5 – 19.3 mm/yr at Box Canyon. The estimated slip rates are geological rates, as they do not include far-field slip, as do geodetic rates; for example, the current ~20 ± 3 mm/yr rate on the sSAF (Fialko, 2006). Because our measurements were collected only along the main trace of the sSAF (Figure 1) and do not account for slip on nearby distributed faults our rate is certainly a minimum and therefore, not comparable to higher geodetic rates. Creep accounts for ~2-4 mm/yr of this rate, which has been shown to be typical for the southern SAF for approximately the last 300 years (Sieh and Williams, 1990). The rates at our sites overlap with slip rates between ~12 and 22 mm/yr, although higher than the preferred estimate of ~14 – 17 mm/yr, for the Mission Creek strand of the sSAF at Biskra Palms (Behr et al., 2010). Our rates are at the upper limit of the 15.9 ± 3.4 mm/yr slip rate determined from an offset alluvial fan southeast of Biskra Palms (van der Woerd et al., 2006). Additionally, the rate in this study coincides with the middle Holocene slip rate of 14 – 20 mm/yr derived from offset boulders and radiocarbon dates on desert varnish and the previous Mecca Hills slip rate of 16 – 21 mm/yr determined by Dingler et al. (2016).

Conclusions

The data and related interpretations indicate that our Mecca Hills and Box Canyon fault segments have experienced large events with an average of 2.7 – 2.9 meters of displacement per event for the past 4 earthquakes. There seems to be no relationship connecting time between large earthquakes and amount of slip that occurs in the next event. We suggest it is less likely that the current ~300-year open interval is resulting in a buildup of seismic moment that may result in an unusually large earthquake.

References Cited

Behr, W.M. et al., 2010, Uncertainties in slip-rate estimates for the Mission Creek strand of the southern San Andreas fault at Biskra Palms Oasis, southern California: Geological Society of America Bulletin, v. 122, p. 1360–1377, doi:10.1130/B30020.1.

Blanton, Chelsea M., Rockwell, Thomas K., Gontz, Allen, and Kelly, Joshua T., 2018, Earthquake Slip, Hurricanes, and Rill Formation – Drone-based DEMs and Orthomosaics from very High-resolution SfM Imagery along the Southern San Andreas Fault, Coachella Valley, California, Geological Society of America Abstracts with Programs. Vol. 50, No. 6, doi: 10.1130/abs/2018AM-317665

Blanton, C.M., Rockwell, T.K., Gontz, A., and Kelly, J. (2018, 08). Analysis of Offset Stream Channels – Deconstructing Creep and Coseismic Slip Components Using Very High Resolution SfM Imagery,

Southern San Andreas Fault, Coachella Valley, California. Poster Presentation at 2018 SCEC Annual Meeting.

Climate Report – National Weather Service, Thermal Airport CA Climate Summary for 14 February 2019. Web. 3 April 2019. https://w2.weather.gov/climate/index.php?wfo=sgx

Dingler, J., Driscoll, N., Seitz, G., and Kent, G., 2016, New quantitative constraints on Holocene slip rate and surface displacement along the southern San Andreas fault in the Mecca Hills using ground based terrestrial laser scanning: in Anderson, R. L., and Ferriz, H., Applied Geology in California: Association of Environmental and Engineering Geologists Special Publication, 26, 809-832.Fattaruso, L., Cooke, M.L., and Dorsey, R., 2014, Sensitivity of uplift patterns to dip of the San Andreas fault in the Coachella Valley, California: Geosphere, v. 10, p. 1235–1246, doi:10.1130/GES01050.1.

Fialko, Y., 2006, Interseismic strain accumulation and the earthquake potential on the southern San Andreas fault system: Nature, v. 441, p. 968–971, doi:10.1038/nature04797.

Lindsey, E.O., Fialko, Y., Bock, Y., Sandwell, D.T., and Bilham, R., 2014, Localized and distributed creep along the southern San Andreas Fault: Journal of Geophysical Research: Solid Earth, v. 119, p. 7909–7922, doi:10.1002/2014JB011275.

Philibosian, B., Fumal, T., and Weldon, R., 2011, San Andreas Fault Earthquake Chronology and Lake Cahuilla History at Coachella, California: Bulletin of the Seismological Society of America, v. 101, p. 13–38, doi:10.1785/0120100050.

Rockwell, T.K., Meltzner, A.J., and Haaker, E.C., 2018, Dates of the Two Most Recent Surface Ruptures on the Southernmost San Andreas Fault Recalculated by Precise Dating of Lake Cahuilla Dry PeriodsDates of the Two Most Recent Surface Ruptures on the Southernmost SAF Recalculated: Bulletin of the Seismological Society of America, v. 108, p. 2634–2649, doi:10.1785/0120170392.

Rockwell, T. K., and Pinault, C. T., 1986, Holocene slip events of the southern Elsinore fault, Coyote Mountains, southern California, in Neotectonics and Faulting in Southern California: Geological Society of American Guidebook for the Cordilleran Section Meeting in Los Angeles, 193-196.

Rockwell, T.K., Meltzner, A.J., and Haaker, E.C., 2018, Dates of the Two Most Recent Surface Ruptures on the Southernmost San Andreas Fault Recalculated by Precise Dating of Lake Cahuilla Dry Periods: Bulletin of the Seismological Society of America, v. 108, p. 2634– 2649, doi:10.1785/0120170392.

Sieh, K.E., and Williams, P.L., 1990, Behavior of the southernmost San Andreas Fault during the past 300 years: Journal of Geophysical Research: Solid Earth, v. 95, p. 6629–6645, doi:10.1029/JB095iB05p06629.

Turner, D., Lucieer, A., and Watson, C., 2012, An Automated Technique for Generating Georectified Mosaics from Ultra-High Resolution Unmanned Aerial Vehicle (UAV) Imagery, Based on Structure from Motion (SfM) Point Clouds: Remote Sensing, v. 4, p. 1392–1410, doi:10.3390/rs4051392.

van der Woerd, J., Klinger, Y., Sieh, K., Tapponnier, P., Ryerson, F.J., and Mériaux, A.-S., 2006, Long-term slip rate of the southern San Andreas Fault from ^{10}Be-^{26}Al surface exposure dating of an offset alluvial fan: Journal of Geophysical Research, v. 111, doi:10.1029/2004JB003559.

Weldon, R, Rockwell, T.K., McCalpin, J., 1996, Chapter 6 Paleoseismology of Strike-Slip Tectonic Environments. International Geophysics. 95. 421-496. 10.1016/S0074-6142(09)95006-9.